12

Projectile Penetration into Semi-infinite Target

12.1 Introduction

A lot of research work has been conducted on impact and penetration analysis. The penetration studies include various lab and field tests, analytical derivations and numerical simulations. Early works were mainly experimental studies. In the last three decades, analytical and numerical tools have been used increasingly as a substitute for costly experiments. The critical issue in an analytical penetration model is to formulate properly the resultant penetration resistance force applied on the missile by the target medium. The most well-known resistance function is based on the so-called dynamic cavity expansion theory. The theory was pioneered by Bishop et al. (1945), who developed the equations for the quasi-static expansion of cylindrical and spherical cavities and estimated forces on conical nose punches pushed slowly into metal targets. Later Hill (1950) and Hopkins (1960) derived and discussed the dynamic and spherically symmetric cavity-expansion equations for an incompressible target material.

The cavity expansion theory was further developed by Luk and Forrestal (1987), Forrestal and Tzou (1997), and Mastilovic and Krajcinovic (1999) to model the penetration of projectiles through soil, porous rock, ceramic and concrete targets. An overview on projectile penetration into geological targets was given by Heuze (1990). Li QM (2005) summarized the recent progress in the penetration mechanics of a hard missile and extended Forrestal's concrete penetration model to missiles of general nose shapes.

By comparison with the analytical results derived from the cylindrical and spherical cavity expansion theories, it is found that the cylindrical assumption gives closer results to test data for low and medium velocity impacts. Tresca criterion and Huber-von Mises criterion were often used for penetration problems of metallic targets, and the Mohr-Coulomb strength theory was used for penetration problems of geomaterials (Longcope and Forrestal, 1983). The selection of failure criteria is of great importance (Zukas et al.,

1982). To reflect the strength difference effect and the effect of failure criteria, the unified strength theory (Yu, 1992; 2004) has been adopted in penetration analysis for both metallic and geological targets (Li and Yu, 2000; Li, 2001; Wei and Yu, 2002; Wei, 2002; Wang et al., 2004; 2005).

The present chapter firstly presents the spatial axisymmetric form of the unified strength theory as the failure condition of target materials in Section 12.2. The governing differential equations for concrete targets are summarized in Section 12.3. The cylindrical cavity expansion model is then applied to incompressible and compressible materials in Sections 12.4. Explicit forms of the pressure on the cavity expansion surface and the cavity expansion velocity are derived in Section 12.5. Section 12.6 gives the resistance force on different nose shapes of the projectile, which is simplified as a rigid body. The penetration depth of the projectile is obtained and compared with test results available in the published literature in Section 12.7.

12.2 Spatial Axisymmetric Form of Unified Strength Theory

There are four stress components σ_r, σ_θ, σ_z and τ_{rz} in a spatial axisymmetric problem. The other components, namely, $\tau_{r\theta}$ and $\tau_{\theta z}$, are zero. According to the spatial axisymmetric unified characteristics line theory (Yu et al., 2001), the stress σ_2 can be expressed as

$$\sigma_2 = \sigma_3 + m\left(\frac{\sigma_1 + \sigma_3}{2} - \sigma_3\right), \tag{12.1}$$

where m is a parameter and $0 \leqslant m \leqslant 2$. When m=0 and m =2, Eq.(12.1) is the Haar-von Karman complete plastic condition. If we define

$$P = \frac{\sigma_1 + \sigma_3}{2},\ R = \frac{\sigma_1 - \sigma_3}{2}, \tag{12.2}$$

then

$$\sigma_1 = P + R,\ \sigma_2 = P + (m-1)R,\ \sigma_3 = P - R. \tag{12.3}$$

The non-zero stress components of an axisymmetric problem can be expressed as

$$\begin{aligned} &\sigma_r = P + R\cos 2\theta,\ \sigma_z = P - R\cos 2\theta, \\ &\tau_{rz} = R\sin 2\theta,\ \sigma_\theta = P + (m-1)R, \end{aligned} \tag{12.4}$$

where θ is the angle between the directions of the maximum principal stress and axis r.

Since $m-1 \leqslant \sin\varphi_0$, that is $\sigma_2 \leqslant P - R\sin\varphi_0$, the unified strength theory (UST) has an expression with respect to the internal friction angle φ_0 and cohesion C_0,

$$\begin{aligned} F &= \sigma_1 - \frac{1-\sin\varphi_0}{(1+b)(1+\sin\varphi_0)}(b\sigma_2+\sigma_3) = \frac{2C_0\cos\varphi_0}{1+\sin\varphi_0}, \\ &\text{when} \quad \sigma_2 \leqslant \frac{1}{2}(\sigma_1+\sigma_3) + \frac{\sin\varphi}{2}(\sigma_1-\sigma_3), \end{aligned} \tag{12.5a}$$

$$\begin{aligned} F' &= \frac{1}{1+b}(\sigma_1+b\sigma_2) - \frac{1-\sin\varphi}{1+\sin\varphi}\sigma_3 = \frac{2C_0\cos\varphi_0}{1+\sin\varphi_0}, \\ &\text{when} \quad \sigma_2 \geqslant \frac{1}{2}(\sigma_1+\sigma_3) + \frac{\sin\varphi}{2}(\sigma_1-\sigma_3). \end{aligned} \tag{12.5b}$$

Then, there is

$$R = -\frac{2(1+b)\sin\varphi_0}{2(1+b)+mb(\sin\varphi_0-1)}P + \frac{2(1+b)C_0\cos\varphi_0}{2(1+b)+mb(\sin\varphi_0-1)}. \tag{12.6}$$

The above equation can be rewritten as (Yu et al., 1997; 2001)

$$R = -P\sin\varphi_{\text{uni}} + C_{\text{uni}}\cos\varphi_{\text{uni}}, \tag{12.7}$$

where the unified strength parameters C_{uni} and φ_{uni} were proposed and derived by Yu et al. in 1997 and 2001. These two parameters are referred as the unified cohesion and unified internal friction angle corresponding to the UST respectively. Their relations to the material constants C_0 and φ_0 can be written as (Yu et al., 1997; 2001)

$$\sin\varphi_{\text{uni}} = \frac{2(1+b)\sin\varphi_0}{2(1+b)+mb(\sin\varphi_0-1)}, \tag{12.8}$$

$$C_{\text{uni}} = \frac{2(1+b)C_0\cos\varphi_0}{2(1+b)+mb(\sin\varphi_0-1)} \cdot \frac{1}{\cos\varphi_{\text{uni}}}. \tag{12.9}$$

Denoting compressive stress as P, Eq.(12.7) can be expressed as (Yu et al., 1997; 2001)

$$R = P\sin\varphi_{\text{uni}} + C_{\text{uni}}\cos\varphi_{\text{uni}}. \tag{12.10}$$

12.3 Fundamental Equations for Concrete Targets

12.3.1 Conservation Equations

In cylindrical coordinates, the conservation equations of momentum and mass for the target materials can be expressed as

$$\frac{\partial v}{\partial r} + \frac{v}{r} = -\frac{1}{\rho}\frac{\mathrm{d}\rho}{\mathrm{d}t}, \tag{12.11}$$

$$\frac{\partial \sigma_r}{\partial r} + \frac{\sigma_r - \sigma_\theta}{r} = -\rho\frac{\mathrm{d}v}{\mathrm{d}t}, \tag{12.12}$$

where v is the radial velocity of a particle in the target material and v is positive if it is in the outward direction.

12.3.2 Relation between Pressure and Bulk Strain

If the material is compressive, the relation between pressure and bulk strain can be expressed as

$$P = K\eta = K(1 - \frac{\rho_0}{\rho}), \tag{12.13}$$

where η is the bulk strain, K is the bulk modulus, P is the hydrostatic pressure and can be written as

$$P = \frac{1}{3}(\sigma_r + \sigma_\theta + \sigma_z). \tag{12.14}$$

For the problem of cavity expansions, the relation among stresses is

$$\sigma_z = \nu\,(\sigma_r + \sigma_\theta) \quad \text{in elastic zone,} \tag{12.15a}$$

$$\sigma_z = \frac{1}{2}\,(\sigma_r + \sigma_\theta) \quad \text{in plastic zone.} \tag{12.15b}$$

Eqs.(12.15a) and (12.15b) are applied respectively for the elastic zone and plastic zone when material is compressible, while only Eq. (12.15b) is used when material is incompressible.

12.3.3 Failure Criterion Expressed by σ_r and σ_θ

The UST is used as the failure condition for the target material in this chapter. According to the axisymmetric stress state of the target material impacted and penetrated by a long rod, Eq.(12.10) has another form of

$$\sigma_r - \sigma_\theta = A_{\mathrm{uni}}\sigma_r + B_{\mathrm{uni}}, \tag{12.16}$$

where

$$A_{\mathrm{uni}} = \frac{2\sin\varphi_{\mathrm{uni}}}{1 + \sin\varphi_{\mathrm{uni}}},\ B_{\mathrm{uni}} = \frac{2C_{\mathrm{uni}}\cos\varphi_{\mathrm{uni}}}{1 + \sin\varphi_{\mathrm{uni}}}.$$

12.3.4 Interface Conditions

The target medium can be divided into four zones during the cavity expansion, i.e., a plastic zone, a radial cracked zone, an elastic zone and an undisturbed zone. At the two interfaces between the plastic and radial cracked zones, radial cracked and elastic zones, the Hugoniot jump conditions are valid. According to the conservation of mass and momentum across the interface, there are

$$[\rho(v - c_J)] = 0, \tag{12.17}$$

$$[\sigma_r + \rho v(v - c_J)] = 0, \tag{12.18}$$

where the expression $[G] = G^+ - G^-$ stands for the magnitude of the discontinuity of the square-bracketed variable across the wave front (interface) that propagates with an interface velocity of c_J. The above equations can also be rewritten as

$$\rho_1(v_1 - c_J) = \rho_2(v_2 - c_J), \tag{12.19}$$

$$\sigma_2 - \sigma_1 = \rho_1(c_J - v_1)(v_2 - v_1). \tag{12.20}$$

12.4 Cylindrical Cavity Expansion Analysis

A cylindrical symmetric cavity expands with velocity v_r from an initial radius of zero when the target is impacted and penetrated by a long rod (Fig.12.1). In Fig.12.2, c is the interface velocity between the plastic and radial cracked zones; c_1 is the interface velocity between the radial cracked and elastic zones; c_d is the elastic dilatation velocity. The stress in the plastic zone ($v_r t \leqslant r \leqslant ct$) has reached the yield surface of the unified strength theory. Because geomaterials are always very weak in tension, radial cracks adjacent to the plastic zone are often observed in a penetration process for targets made of geomaterials. The formation and the magnitude of the area for a cracked zone or a damaged zone depend on the circumferential tensile stress. If the circumferential stress exceeds the tensile strength of the target material, a radial cracked zone forms. The range of the radial cracked zone can be represented by $ct < r \leqslant c_1 t$. The elastic zone is in the range of $c_1 t < r \leqslant c_d t$; and the undisturbed zone is in the range of $r > c_d t$. Defining a dimensionless variable of $\xi = r/ct$, the four different zones can be categorized in Fig.12.3.

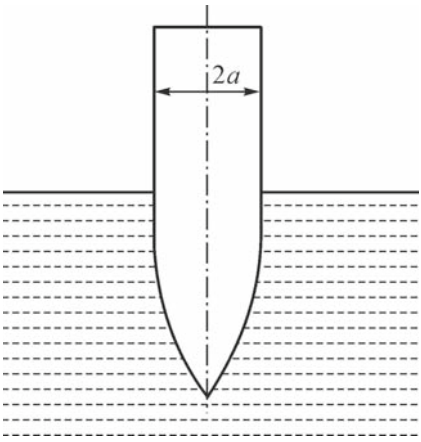

Fig. 12.1. Penetration by a long rod

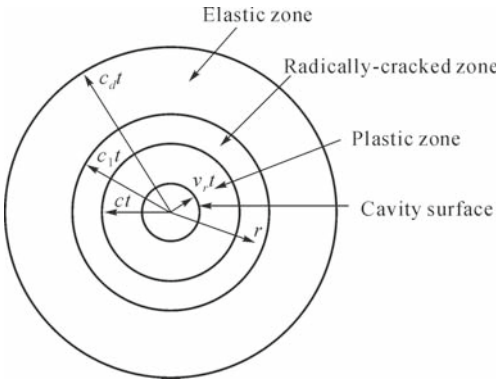

Fig. 12.2. Different zones of target material

12.4.1 Elastic Zone ($c_1 t \leqslant r \leqslant c_d t$, $\beta_1/\beta \leqslant \xi \leqslant 1/\alpha$)

In the elastic zone, the target materials satisfy the linear stress-strain relations. According to the generalized Hooke's law,

$$\sigma_r = -\frac{E}{(1-2\nu)(1+\nu)}\left[(1-\nu)\frac{\partial u}{\partial r} + \nu\frac{u}{r}\right], \tag{12.21}$$

$$\sigma_\theta = -\frac{E}{(1-2\nu)(1+\nu)}\left[\nu\frac{\partial u}{\partial r} + (1-\nu)\frac{u}{r}\right], \tag{12.22}$$

where E and ν are the modulus of elasticity and Poisson's ratio; u is the radial displacement. The normal stresses are positive in compression for convenient formulation.

The conservation equation of momentum can be expressed as

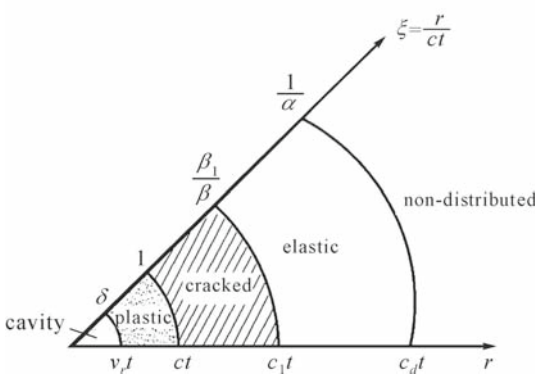

Fig. 12.3. Dimensionless expression of the four zones

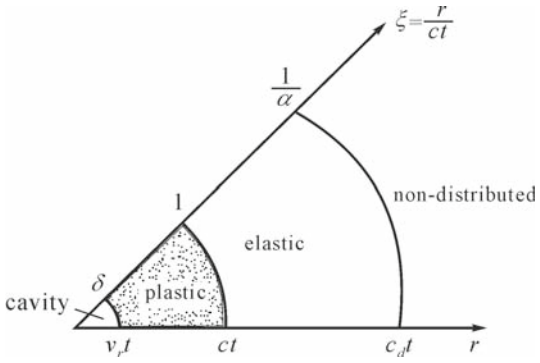

Fig. 12.4. Dimensionless expression of the three zones

$$\frac{\partial \sigma_r}{\partial r} + \frac{\sigma_r - \sigma_\theta}{r} = -\rho \left(\frac{\partial \nu}{\partial t} + \nu \frac{\partial \nu}{\partial r} \right). \tag{12.23}$$

Substituting Eqs.(12.21) and (12.22) into Eq.(12.23), we obtain

$$\frac{\partial^2 u}{\partial r^2} + \frac{1}{r}\frac{\partial u}{\partial r} - \frac{u}{r^2} = \frac{1}{c_d^2}\frac{\mathrm{d}^2 u}{\mathrm{d}t^2}, \tag{12.24}$$

where c_d is the elastic wave velocity in the semi-infinite medium and

$$c_d = \sqrt{\frac{E(1-\nu_0)}{(1+\nu_0)(1-2\nu_0)\rho_0}}. \tag{12.25}$$

Defining

$$u = \frac{\bar{u}}{ct}, \tag{12.26}$$

Eq.(12.24) can be rewritten as

$$(1-\alpha^2\xi^2)\frac{\mathrm{d}^2\bar{u}}{\mathrm{d}\xi^2}+\frac{1}{\xi}\frac{\mathrm{d}\bar{u}}{\mathrm{d}\xi}-\frac{1}{\xi^2}\bar{u}=0, \tag{12.27}$$

where $\alpha = c/c_d$.

Defining

$$z=\alpha\xi, \bar{u}=z\phi, F=\frac{\mathrm{d}\phi}{\mathrm{d}z}, \tag{12.28}$$

then

$$\begin{cases} \dfrac{\mathrm{d}\bar{u}}{\mathrm{d}\xi}=\alpha\phi+\alpha zF, \\ \dfrac{\mathrm{d}^2\bar{u}}{\mathrm{d}\xi^2}=2\alpha^2F+\alpha^2z\dfrac{\mathrm{d}F}{\mathrm{d}z}. \end{cases} \tag{12.29}$$

Eq.(12.27) can be simplified into a first-order differential equation with reference to Eq.(12.29). Integrating Eq.(12.27), we obtain

$$\bar{u}=A\alpha\xi+\left[\frac{\alpha\xi}{2}\ln\frac{1+\sqrt{1-\alpha^2\xi^2}}{\alpha\xi}-\frac{\sqrt{1-\alpha^2\xi^2}}{2\alpha\xi}\right]\cdot B, \tag{12.30}$$

where A and B are integration constants that can be determined by considering the following boundary conditions:

$$\bar{u}(\xi=\frac{1}{\alpha})=0, \tag{12.31}$$

$$\sigma_\theta(\xi=\frac{\beta_1}{\beta})=-\sigma_t, \tag{12.32}$$

where Eq.(12.31) indicates that the radial displacement is zero at the interface of the elastic and undistributed zones; Eq.(12.32) indicates that the circumferential stress reaches the tensile strength at the interface of the elastic and radial crack zones.

With reference to Eq.(12.30) and Eq.(12.31),

$$A=0. \tag{12.33}$$

The displacement distribution in the elastic zone is then derived as

$$\bar{u}=\left[\frac{\alpha\xi}{2}\ln\frac{1+\sqrt{1-\alpha^2\xi^2}}{\alpha\xi}-\frac{\sqrt{1-\alpha^2\xi^2}}{2\alpha\xi}\right]\cdot B. \tag{12.34}$$

From Eq.(12.34),

$$\frac{\bar{u}}{\xi} = \left[\frac{\alpha}{2}\ln\frac{1+\sqrt{1-\alpha^2\xi^2}}{\alpha\xi} - \frac{\sqrt{1-\alpha^2\xi^2}}{2\alpha\xi^2}\right]\cdot B, \tag{12.35}$$

$$\frac{\partial\bar{u}}{\partial\xi} = \left[\frac{\alpha}{2}\ln\frac{1+\sqrt{1-\alpha^2\xi^2}}{\alpha\xi} + \frac{\sqrt{1-\alpha^2\xi^2}}{2\alpha\xi^2}\right]\cdot B. \tag{12.36}$$

Defining

$$\bar{\sigma}_r = \frac{\sigma_r}{K},\ \bar{\sigma}_\theta = \frac{\sigma_\theta}{K},\ \bar{\sigma}_t = \frac{\sigma_t}{K}, \tag{12.37}$$

the dimensionless circumferential stress and radial stress in the elastic zone can be derived from Eqs.(12.21) and (12.22),

$$\bar{\sigma}_\theta = -\frac{3}{1+\nu}\left[\frac{\alpha}{2}\ln\frac{1+\sqrt{1-\alpha^2\xi^2}}{\alpha\xi} - \frac{(1-2\nu)\sqrt{1-\alpha^2\xi^2}}{2\alpha\xi^2}\right]\cdot B, \tag{12.38}$$

$$\bar{\sigma}_r = -\frac{3}{1+\nu}\left[\frac{\alpha}{2}\ln\frac{1+\sqrt{1-\alpha^2\xi^2}}{\alpha\xi} + \frac{(1-2\nu)\sqrt{1-\alpha^2\xi^2}}{2\alpha\xi^2}\right]\cdot B. \tag{12.39}$$

The integration constant B can be obtained from Eq.(12.32) with reference to Eq.(12.38),

$$B = \frac{1+\nu}{3}\sigma_t\left[\frac{\alpha}{2}\ln\frac{1+\sqrt{1-\alpha^2\left(\beta_1/\beta\right)^2}}{\alpha\left(\beta_1/\beta\right)} - \frac{(1-2\nu)\sqrt{1-\alpha^2\left(\beta_1/\beta\right)^2}}{2\alpha\left(\beta_1/\beta\right)^2}\right]^{-1}. \tag{12.40}$$

Defining a dimensionless radial velocity as

$$\bar{\nu}(\xi) = \frac{\bar{\nu}}{c}, \tag{12.41}$$

Eq.(12.34) yields

$$\bar{\nu}(\xi) = \left[-\frac{\sqrt{1-\alpha^2\xi^2}}{\alpha\xi}\right]\cdot B. \tag{12.42}$$

At the interface of elastic-radial cracked zones, i.e., $\xi = \beta_1/\beta$, the radial stress, the circumferential stress and the velocity in the elastic zone are

$$\bar{\sigma}_{r1} = -\frac{3}{1+\nu}\left[\frac{\alpha}{2}\ln\frac{1+\sqrt{1-\alpha^2\left(\beta_1/\beta\right)^2}}{\alpha\left(\beta_1/\beta\right)} + \frac{(1-2\nu)\sqrt{1-\alpha^2\left(\beta_1/\beta\right)^2}}{2\alpha\left(\beta_1/\beta\right)^2}\right]\cdot B, \tag{12.43}$$

$$\bar{\sigma}_{\theta 1} = -\frac{3}{1+\nu}\left[\frac{\alpha}{2}\ln\frac{1+\sqrt{1-\alpha^2\left(\beta_1/\beta\right)^2}}{\alpha\left(\beta_1/\beta\right)} - \frac{(1-2\nu)\sqrt{1-\alpha^2\left(\beta_1/\beta\right)^2}}{2\alpha\left(\beta_1/\beta\right)^2}\right]\cdot B, \tag{12.44}$$

$$\bar{\nu}_1(\xi) = \left[-\frac{\sqrt{1-\alpha^2\left(\beta_1/\beta\right)^2}}{\alpha\left(\beta_1/\beta\right)}\right]\cdot B. \tag{12.45}$$

12.4.2 Interface of Elastic-cracked Zones ($r = c_1 t$, $\xi = \beta_1/\beta$)

Defining at the interface the dimensionless radial stress and radial velocity in the cracked zone as $\bar{\sigma}_{r2}$ and $\bar{\nu}_2$, respectively, with reference to the Hugoniot jump condition,

$$\rho_1\left(\bar{\nu}_1 - \frac{\beta_1}{\beta}\right) = \rho_2\left(\bar{\nu}_2 - \frac{\beta_1}{\beta}\right), \tag{12.46}$$

$$\bar{\sigma}_{r2} = \bar{\sigma}_{r1} + \frac{\rho_1}{\rho_0}\beta^2\left(\frac{\beta_1}{\beta} - \bar{\nu}_1\right)\left(\bar{\nu}_2 - \bar{\nu}_1\right), \tag{12.47}$$

where ρ_1 and ρ_2 are the density of materials in the elastic and crack zones respectively.

According to the pressure-bulk strain relation, in the elastic zone,

$$\frac{(1+\nu)\sigma_r + (2-\nu)\sigma_\theta}{3} = K\left(1 - \frac{\rho_0}{\rho}\right). \tag{12.48}$$

Since the circumferential stress is zero in the cracked zone, the above equation can be rewritten as

$$\frac{1+\nu}{3}\sigma_r = K\left(1 - \frac{\rho_0}{\rho}\right). \tag{12.49}$$

At the interface, the circumferential stress in the elastic zone reaches the tensile strength, which implies

$$\bar{\sigma}_{\theta 1} = -\bar{\sigma}_t. \tag{12.50}$$

Substituting the above equation into Eq.(12.48), the radial stress in the elastic zone near to the interface can be expressed as

$$\bar{\sigma}_{r1} = \frac{2-\nu}{1+\nu}\bar{\sigma}_t + \frac{3}{1+\nu}\left(1 - \frac{\rho_0}{\rho_1}\right). \tag{12.51}$$

From Eq.(12.49), the radial stress in the cracked zone near to the interface can be derived as

$$\bar{\sigma}_{r2} = \frac{3}{1+\nu}\left(1 - \frac{\rho_0}{\rho_2}\right). \tag{12.52}$$

Substituting Eq.(12.51) into Eq.(12.47),

$$\bar{\sigma}_{r2} = \bar{\sigma}_{r1} + \frac{3(\beta_1 - \beta\bar{\nu}_1)(\beta\bar{\nu}_2 - \beta\bar{\nu}_1)}{3 - (1+\nu)(\bar{\sigma}_{r1} - \bar{\sigma}_t)}. \tag{12.53}$$

Putting the expression of ρ_1 and ρ_2 from Eqs.(12.51) and (12.52) into Eq.(12.46),

$$\beta\bar{\nu}_2 = \beta_1 + \frac{3 - \bar{\sigma}_{r2}(1+\nu)}{3 - (\bar{\sigma}_{r1} - \bar{\sigma}_t)(1+\nu)}(\beta\bar{\nu}_1 - \beta_1). \tag{12.54}$$

12.4.3 Radial Cracked Zone ($ct \leqslant r \leqslant c_1 t$, $1 \leqslant \xi \leqslant \beta_1/\beta$)

When the circumferential stress reaches the tensile strength, the radial cracks occur. Once the radial cracks occur, σ_θ diminishes immediately to zero. The conservation equations of mass and momentum can be expressed as

$$\frac{\partial \nu}{\partial r} + \frac{\nu}{r} = -\frac{1}{\rho}\frac{\mathrm{d}\rho}{\mathrm{d}t}, \tag{12.55}$$

$$\frac{\partial \sigma_r}{\partial r} + \frac{\sigma_r}{r} = -\rho\left(\frac{\partial \nu}{\partial t} + \nu\frac{\partial \nu}{\partial r}\right). \tag{12.56}$$

According to the pressure-bulk strain relation,

$$P = \frac{1+\nu}{3}\sigma_r = K\left(1 - \frac{\rho_0}{\rho}\right) = K\eta. \tag{12.57}$$

Putting Eq.(12.57) into Eqs.(12.55) and (12.56) respectively,

$$\frac{\partial \nu}{\partial r} + \frac{\nu}{r} = -\frac{1+\nu}{3K(1-\eta)}\frac{\mathrm{d}\sigma_r}{\mathrm{d}t}, \tag{12.58}$$

$$\frac{\partial \sigma_r}{\partial r} + \frac{\sigma_r}{r} = -\frac{\rho_0}{1-\eta}\left(\frac{\partial \nu}{\partial t} + \nu\frac{\partial \nu}{\partial r}\right). \tag{12.59}$$

Because the bulk strain is very small, there is $1 - \eta \approx 1$. The above equations can be rewritten as

$$\begin{cases} \dfrac{\mathrm{d}\bar{\nu}}{\mathrm{d}\xi} + \dfrac{\bar{\nu}}{\xi} = \dfrac{1+\nu}{3}\xi\dfrac{\mathrm{d}\bar{\sigma}_r}{\mathrm{d}\xi}, \\ \dfrac{\mathrm{d}\bar{\sigma}_r}{\mathrm{d}\xi} + \dfrac{\bar{\sigma}_r}{\xi} = \beta^2\xi\dfrac{\mathrm{d}\bar{\nu}}{\mathrm{d}\xi}. \end{cases} \tag{12.60}$$

Integrating Eq.(12.60), we obtain

$$\bar{\sigma}_r(\xi) = -\frac{D_1}{\xi} + D_2, \tag{12.61}$$

$$\bar{\nu}(\xi) = -\frac{D_2}{\beta^2\xi} + \frac{1+\nu}{3}D_1, \tag{12.62}$$

where D_1 and D_2 are the integration constants that can be determined with application of boundary conditions.

At the interface of the cracked and plastic zones ($r = ct$, $\xi = 1$), defining radial stress and radial velocity in the cracked zone $\bar{\sigma}_{r3}$ and $\bar{\nu}_3$, respectively, the boundary conditions can be expressed as

$$r = ct(\xi = 1), \quad \begin{cases} \bar{\sigma}_r(\xi = 1) = \bar{\sigma}_{r3} = \frac{\bar{B}_t}{1-A_t}, \\ \bar{\nu}(\xi = 1) = \bar{\nu}_3, \end{cases} \tag{12.63}$$

$$r = c_1 t(\xi = \beta_1/\beta), \quad \begin{cases} \bar{\sigma}_r(\xi = \beta_1/\beta) = \bar{\sigma}_{r2}, \\ \\ \bar{\nu}(\xi = \beta_1/\beta) = \bar{\nu}_2. \end{cases} \tag{12.64}$$

From Eqs.(12.61) and (12.63),

$$-D_1 + D_2 = \frac{\bar{B}_t}{1 - A_t}. \tag{12.65}$$

The radial stress and the radial velocity in the cracked zone adjacent to the interface of the cracked and elastic zones ($r = c_1 t$, $\xi = \beta_1/\beta$) can be expressed as

$$\bar{\sigma}_{r2} = -\frac{D_1}{\beta_1/\beta} + D_2, \tag{12.66}$$

$$\bar{\nu}_2 = -\frac{D_2}{\beta_1\beta} + \frac{1+\nu}{3}D_1, \tag{12.67}$$

the integration constants D_1, D_2 can then be expressed as

$$D_1 = \frac{3\beta_1(\bar{\sigma}_{r2} + \beta_1\beta\bar{\nu}_2)}{\beta[\beta_1^2(1+\nu) - 3]}, \tag{12.68}$$

$$D_2 = \frac{\beta_1^2(1+\nu)\bar{\sigma}_{r2} + 3\beta_1\beta\bar{\nu}_2}{\beta_1^2(1+\nu) - 3}. \tag{12.69}$$

Putting Eqs.(12.68) and (12.69) into Eq.(12.65),

$$\frac{\bar{B}_t}{1-A_t} = -\frac{3\beta_1(\bar{\sigma}_{r2}+\beta_1\beta\bar{\nu}_2)}{\beta[\beta_1^2(1+\nu)-3]} + \frac{\beta_1^2(1+\nu)\bar{\sigma}_{r2}+3\beta_1\beta\bar{\nu}_2}{\beta_1^2(1+\nu)-3}. \tag{12.70}$$

The velocity in the cracked zone adjacent to the cracked-elastic zones interface can be written as

$$\bar{\nu}_3 = -\frac{1}{\beta^2}\frac{\beta_1^2(1+\nu)\bar{\sigma}_{r2}+3\beta\beta_1\bar{\nu}_2}{\beta^2(1+\nu)-3} + \frac{\beta_1(1+\nu)(\bar{\sigma}_{r2}+\beta\beta_1\bar{\nu}_2)}{\beta[\beta_1^2(1+\nu)-3]}. \tag{12.71}$$

12.4.4 Interface of the Plastic and Cracked Zones ($r = ct$, $\xi = 1$)

Defining $\bar{\sigma}_{r4}$ and $\bar{\nu}_4$ the radial stress and velocity, respectively, in the plastic zone adjacent to the interface, with reference to the Hugoniot jump condition,

$$\rho_4\left(\bar{\nu}_4 - 1\right) = \rho_3\left(\bar{\nu}_3 - 1\right), \tag{12.72}$$

$$\bar{\sigma}_{r4} = \bar{\sigma}_{r3} + \frac{\rho_3}{\rho_0}\beta^2\left(1-\bar{\nu}_3\right)\left(\bar{\nu}_4 - \bar{\nu}_3\right), \tag{12.73}$$

where ρ_4 and ρ_3 are the density in the plastic and cracked zones adjacent to the interface respectively.

From Eq.(12.63),

$$\bar{\sigma}_{r3} = \frac{\bar{B}_{\text{uni}}}{1-A_{\text{uni}}}. \tag{12.74}$$

According to the pressure-bulk strain relation, the following expression can be obtained:

$$\left(1-\frac{\rho_0}{\rho_3}\right) = \frac{1+\nu}{3}\frac{\bar{B}_{\text{uni}}}{1-A_{\text{uni}}}. \tag{12.75}$$

Putting Eq.(12.75) into Eq.(12.73),

$$\bar{\sigma}_{r4} = \bar{\sigma}_{r3} + \frac{3(1-A_{\text{uni}})\beta^2\left(1-\bar{\nu}_3\right)\left(\bar{\nu}_4-\bar{\nu}_3\right)}{3(1-A_{\text{uni}})-(1+\nu)\bar{B}_{\text{uni}}}. \tag{12.76}$$

Based on the unified strength theory, the material in the plastic zone satisfies

$$\bar{\sigma}_r - \bar{\sigma}_\theta = A_{\text{uni}}\bar{\sigma}_r + \bar{B}_{\text{uni}}, \tag{12.77}$$

where

$$A_{\text{uni}} = \frac{2\sin\varphi_{\text{uni}}}{1+\sin\varphi_{\text{uni}}},\ B_{\text{uni}} = \frac{2C_{\text{uni}}\cos\varphi_{\text{uni}}}{1+\sin\varphi_{\text{uni}}}.$$

C_{uni} and φ_{uni} are the unified internal friction angle and unified cohesion, respectively, corresponding to the unified strength theory and they have the form of

$$\sin\varphi_{\text{uni}} = \frac{2(1+b)\sin\varphi_0}{2+b+b\sin\varphi_0}, \tag{12.78}$$

$$C_{\text{uni}} = \frac{2(1+b)c_0\cos\varphi_0}{2+b+b\sin\varphi_0}\cdot\frac{1}{\cos\varphi_{\text{uni}}}. \tag{12.79}$$

At the interface, Eq.(12.77) can be rewritten as

$$\bar{\sigma}_{r4} - \bar{\sigma}_{\theta 4} = A_{\text{uni}}\bar{\sigma}_{r4} + \bar{B}_{\text{uni}}. \tag{12.80}$$

According to the pressure-bulk strain relation,

$$\frac{1}{2}(\bar{\sigma}_{r4} + \bar{\sigma}_{\theta 4}) = 1 - \frac{\rho_0}{\rho_4}. \tag{12.81}$$

From the above equations it derives

$$\rho_4 = \frac{2\rho_0}{2-(2-A_{\text{uni}})\bar{\sigma}_{r4} + \bar{B}_{\text{uni}}}. \tag{12.82}$$

Putting Eq.(12.82) into Eq.(12.72), then there is

$$\bar{\nu}_4 = 1 + \frac{\rho_3(2+\bar{B}_{\text{uni}})(\bar{\nu}_3-1)}{2\rho_0} - \frac{\rho_3(2-A_{\text{uni}})\bar{\sigma}_{r4}(\bar{\nu}_3-1)}{2\rho_0}. \tag{12.83}$$

From Eqs.(12.83) and (12.76), we can get

$$\bar{\sigma}_{r4} = \bar{n}\bar{\sigma}_{r3} + \bar{n}\frac{\rho_3}{\rho_0}\beta^2(\bar{\nu}_3-1)^2\left[1 - \frac{\rho_3(2+\bar{B}_{\text{uni}})}{2\rho_0}\right], \tag{12.84}$$

where

$$\bar{n} = \frac{2\rho_0^2}{2\rho_0^2 - \rho_3^2\beta^2(1-\bar{\nu}_3)^2(2-A_{\text{uni}})}.$$

12.4.5 Plastic Zone ($v_r t \leqslant r \leqslant ct$, $\delta \leqslant \xi \leqslant 1$)

The mass and momentum equations in Eqs.(12.55) and (12.56) are still valid in the plastic zone. The boundary stress and velocity conditions in the plastic zone can be expressed as

$$r = v_r t,\ \bar{\nu}(\xi = \delta) = \delta, \tag{12.85}$$

$$r = ct,\ \begin{cases} \bar{\sigma}_r(\xi = 1) = \bar{\sigma}_{r4}, \\ \bar{\nu}(\xi = 1) = \bar{\nu}_4. \end{cases} \tag{12.86}$$

According to the pressure-bulk strain relation,

$$(\sigma_r + \sigma_\theta) = 2K\left(1 - \frac{\rho_0}{\rho_4}\right) = 2K\eta. \tag{12.87}$$

The material in the plastic zone satisfies the unified strength theory,

$$\sigma_r - \sigma_\theta = A_t\sigma_r + B_t. \tag{12.88}$$

From Eqs.(12.87) and (12.88),

$$\eta = \frac{(2 - A_t)\bar{\sigma}_r - \bar{B}_t}{2}. \tag{12.89}$$

Putting Eqs.(12.87) and (12.88) into the mass and momentum conservation equations, the following differential equations can be derived,

$$\frac{\partial \nu}{\partial r} + \frac{\nu}{r} = -\frac{2 - A_t}{2K(1 - \eta)}\left(\frac{\partial \sigma_r}{\partial t} + \nu\frac{\partial \sigma_r}{\partial r}\right), \tag{12.90}$$

$$\frac{\partial \sigma_r}{\partial r} + \frac{A_t\sigma_r + B_t}{r} = -\frac{\rho_0}{1 - \eta}\left(\frac{\partial \nu}{\partial t} + \nu\frac{\partial \nu}{\partial r}\right). \tag{12.91}$$

The dimensionless expressions of the above equations are

$$\frac{\mathrm{d}\bar{\nu}}{\mathrm{d}\xi} + \frac{\bar{\nu}}{\xi} = -\frac{2 - A_{\mathrm{uni}}}{2(1 - \eta)}(\xi - \bar{\nu})\frac{\mathrm{d}\sigma_r}{\mathrm{d}\xi}, \tag{12.92}$$

$$\frac{\mathrm{d}\bar{\sigma}_r}{\mathrm{d}\xi} + \frac{A_{\mathrm{uni}}\bar{\sigma}_r + \bar{B}_{\mathrm{uni}}}{\xi} = \frac{\beta^2}{1 - \eta}(\xi - \bar{\nu})\frac{\mathrm{d}\bar{\nu}}{\mathrm{d}\xi}. \tag{12.93}$$

Eqs.(12.92) and (12.93) can be rewritten as

$$\frac{\mathrm{d}\bar{\sigma}_r}{\mathrm{d}\xi} = \frac{2(1 - \eta)\left[\beta\bar{\nu}(\beta\xi - \beta\bar{\nu}) + (1 - \eta)(A_{\mathrm{uni}}\bar{\sigma}_r + \bar{B}_{\mathrm{uni}})\right]}{\xi[(2 - A_{\mathrm{uni}})(\beta\xi - \beta\bar{\nu})^2 - 2(1 - \eta)^2]}, \tag{12.94}$$

$$\frac{\mathrm{d}(\beta\bar{\nu})}{\mathrm{d}\xi} = \frac{(1-\eta)\left[(2-A_{\mathrm{uni}})(A_{\mathrm{uni}}\bar{\sigma}_r + \bar{B}_{\mathrm{uni}})(\beta\xi - \beta\bar{\nu}) + 2\beta\bar{\nu}(1-\eta)\right]}{\xi[(2-A_{\mathrm{uni}})(\beta\xi - \beta\bar{\nu})^2 - 2(1-\eta)^2]}. \tag{12.95}$$

Eqs.(12.94) and (12.95) can be solved using the Runge-Kutta method. Defining $y_1 = \bar{\sigma}_r$ and $y_2 = \bar{\nu}$, the boundary conditions can be written as $y_1(0) = \bar{\sigma}_{r4}$ and $y_2(0) = \bar{\nu}_4$. When the stress and velocity in the plastic zone are deduced, Eqs.(12.94) and (12.95) can be expressed in the form

$$\begin{cases} y_1' = f(\xi, y_1, y_2), & y_1(0) = \sigma_{r4}, \\ y_2' = g(\xi, y_1, y_2), & y_2(0) = \bar{\nu}_4. \end{cases} \tag{12.96}$$

The integral domain borders the plastic-cracked zones interface ($\xi = 1$) and the cavity surface ($\xi = \delta$). According to the boundary conditions, when $\xi_n = 1 - n\Delta\xi$, $y_{2n} = \xi_n$. The radial stress and velocity at the cavity surface can be obtained when $\delta = \xi_n$ and $y_1(n) = \bar{\sigma}_r(\delta)$.

The detailed procedures for solving the differential equations are given as follows:

Step 1. Substituting Eqs.(12.43), (12.45), (12.53), and (12.54) into Eq. (12.70), the relation between β_1 and β is deduced.

Step 2. Assuming an initial value for β_1, β can be calculated with reference to the relations between β_1 and β deduced in Step 1.

Step 3. $\bar{\sigma}_{r1}$ and $\bar{\nu}$ are calculated from Eqs.(12.43) and (12.45) with reference to β_1 and β. Putting $\bar{\sigma}_{r1}$ and $\bar{\nu}_1$ into Eqs.(12.53), (12.54), (12.68), (12.69), and (12.71), $\bar{\sigma}_{r2}$ and $\bar{\nu}_2$, the integration constants D_1 and D_2, and $\bar{\nu}_3$ are determined. Putting the above quantities into Eqs.(12.74) and (12.75), $\bar{\sigma}_{r3}$ and $\bar{\rho}_3$ are obtained.

Step 4. Substituting $\bar{\sigma}_{r3}$, $\bar{\rho}_3$, and $\bar{\nu}_3$ into Eqs.(12.84) and (12.83), $\bar{\sigma}_{r4}$ and $\bar{\nu}_4$ are determined.

Step 5. Based on boundary conditions, the differential equation in Eq.(12. 96) is solved from $\xi = 1$ to $\xi = \delta$. The stress and velocity distribution in the plastic zone is then calculated. With application of the boundary conditions, the radial stress and the expansion velocity are obtained.

When the bulk strain is zero, i.e., $\eta = 0$, and $\rho_i = \rho_0$ $(i = 1, ..., 4)$, the solutions for incompressible materials can be deduced from Eqs.(12.21) to (12.96). If the interface velocities c and c_1 are the same, the radial cracked zone disappears and there are only plastic, elastic, and undisturbed zones in the materials.

12.5 Cavity Expansion Pressure and Velocity

With application of the concrete parameters given by Forrestal (1997), i.e., bulk modulus K of 6.7 GPa, compressive strength Y of 130 MPa, elastic modulus E of 11.3 GPa, Poisson's ratio ν of 0.22, tensile strength $\sigma_t = 13$

MPa, density $\rho_0 = 2260$ kg/m^3, according to the derived equations based on the cylindrical cavity expansion theory, the material is considered to be incompressible or compressible. The response of the target can be elastic-plastic or elastic-crack-plastic, respectively.

12.5.1 Incompressible Material

Fig.12.5 illustrates the relation between the radial stress at the cavity surface and the cavity expansion velocity for the elastic-plastic response of the target. From Fig.12.5, the radial stress increases with increasing cavity expansion velocity, the radial stress and the unified strength theory parameter b.

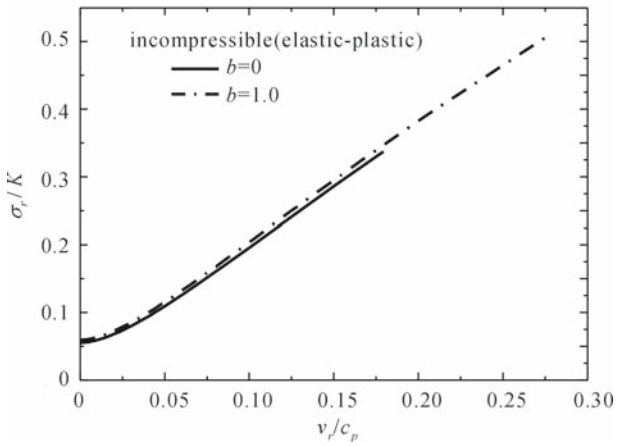

Fig. 12.5. Radial stress versus cavity expansion velocity (incompressible material, elastic-plastic response)

Figs.12.6 and 12.7 plot the curves of the plastic-crack interface velocity c and the elastic-crack interface velocity c_1 versus the cavity expansion velocity v_r for incompressible material for $b = 1.0$ and $b = 0$, respectively. It is shown that for a given velocity v_r, c_1 is higher than c. When $b = 1.0$ and $v_r/(Y/\rho_0)^{1/2} = 0.82$, the curves of c_1 and c intersect, i.e., the cracked zone vanishes at this cavity expansion velocity and there are only elastic and plastic zones in the material. When $b = 0$ and $v_r/(Y/\rho_0)^{1/2} = 0.7$, the curves of c_1 and c also intersect, the response of material shifts from elastic-crack-plastic to elastic-plastic. The current solution with $b = 0$ conforms to the result reported by Forrestal (1997), who applied the spherical cavity expansion theory and discovered that the cracked zone disappears when $v_r/(Y/\rho_0)^{1/2} = 0.71$.

Fig.12.8 illustrates schematically the relation between the radial stress in the cavity surface and the cavity expansion velocity for incompressible materials under elastic-crack-plastic response for $b = 0$ and $b = 1.0$, respectively.

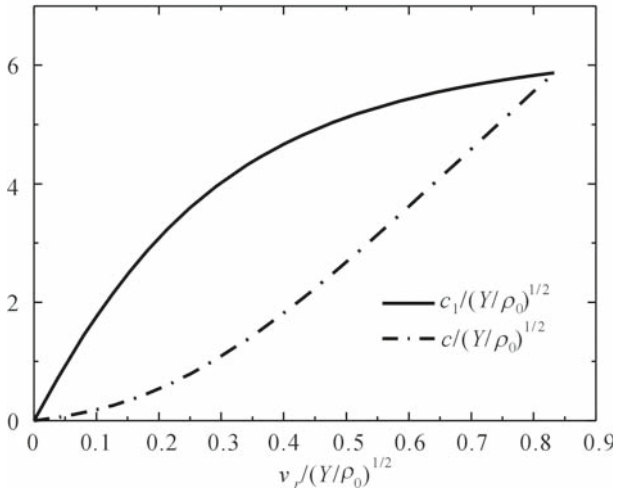

Fig. 12.6. Cavity expansion velocity versus interface velocity (incompressible material, elastic-crack-plastic response, $b = 1.0$)

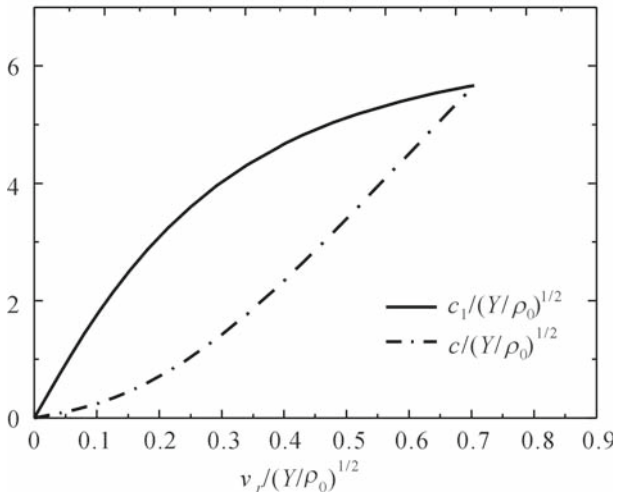

Fig. 12.7. Cavity expansion velocity versus interface velocity (incompressible material, elastic-crack-plastic response, $b = 0$)

The radial stress for $b = 1.0$ is higher than that for $b = 0$. The radial stress increases with increasing cavity expansion velocity. The quasi-static cavity expansion pressure is the radial stress at the cavity surface when $v_r = 0$.

Compared with the results given by Forrestal (1997) which are based on the spherical cavity expansion theory, the radial stress derived based on the cylindrical cavity expansion theory is smaller when the impact velocity is

relatively low. However, it is higher when the impact velocity is relatively high. It agrees with the statements by Forrestal (1997).

Fig.12.9 compares the radial stresses between the elastic-plastic response and the elastic-crack-plastic response for incompressible material. From Fig. 12.9, the stress is higher for the elastic-plastic response when the velocity is lower. When the velocity increases, the stress of the elastic-crack-plastic response gradually transfers to that of elastic-plastic response. Finally, the curves of the two responses intersect.

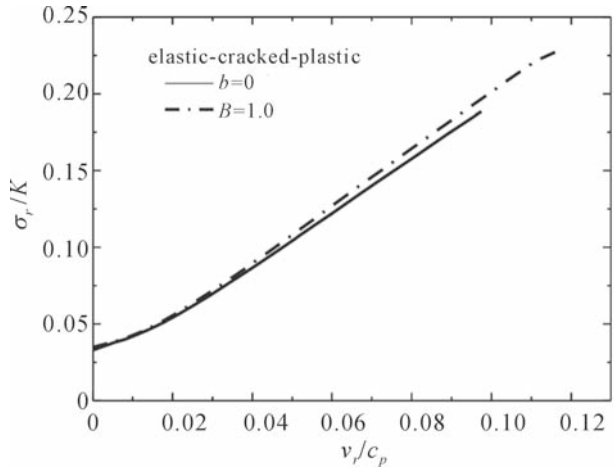

Fig. 12.8. Radial stress at cavity surface versus cavity expansion velocity (incompressible material, elastic-crack-plastic response)

Fig.12.10 shows the curves of elastic-crack interface velocity c_1 versus plastic-crack interface velocity c during the cavity expansion. The curves are different for different parameter b. Fig.12.11 plots the curves of the cavity expansion velocity v_r versus the plastic-crack interface velocity c for incompressible material. Fig.12.12 plots the curves of the radial stress versus the radius for incompressible material under the elastic-crack-plastic response. Fig.12.12 shows that the stress at the cavity surface is the highest and reduces gradually with the increasing radius.

12.5.2 Compressible Material

Figs.12.13 and 12.14 compare the cavity expansion stress of compressible materials with that of incompressible materials under elastic-plastic response for $b = 0$ (Single-shear theory) and $b = 1.0$ (Twin-shear theory) respectively. It is seen that for a given cavity expansion velocity, the cavity expansion surface pressure of incompressible materials is much higher than that of compressible materials.

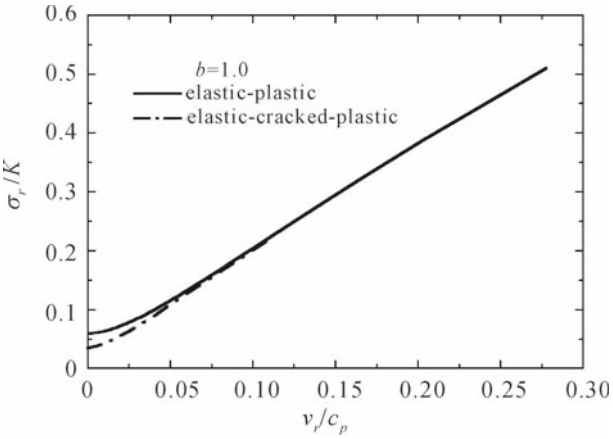

Fig. 12.9. Comparison of radial stress for elastic-plastic and elastic-crack-plastic responses (incompressible material)

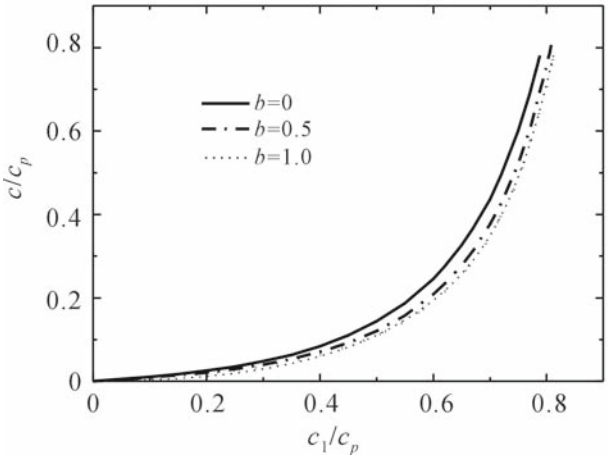

Fig. 12.10. Curves of c_1 versus c for incompressible material

Fig.12.15 illustrate the curves of cavity expansion velocity v_r versus the plastic-crack interface velocity c. From Fig.12.15, for a given v_r, c is the highest when $b = 0$, while it is the lowest when $b = 1.0$. Fig.12.16 plots the relations between the cavity expansion velocity, plastic-crack interface velocity c and plastic-crack interface velocity c_1 for compressible materials with $b = 0.5$. Similar to the incompressible materials, for a given v_r the elastic-crack interface velocity c_1 is higher than the plastic-crack interface velocity c, where $f(\xi, y_1, y_2)$ and $g(\xi, y_1, y_2)$ correspond with Eqs.(12.94) and (12.95). The curves of c_1 and c intersect at the point when $v_r/(Y/\rho_0)^{1/2} =$

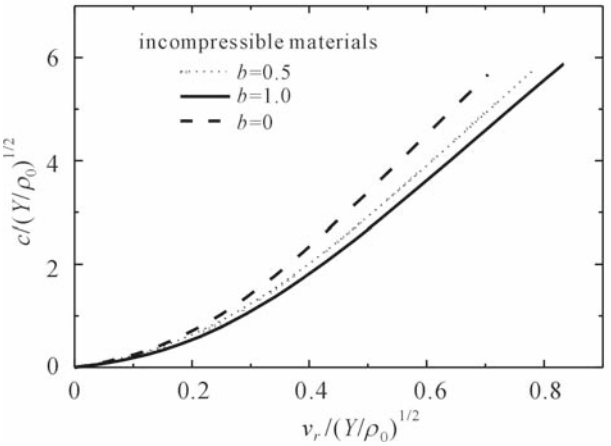

Fig. 12.11. Curves of v_r versus c for incompressible material

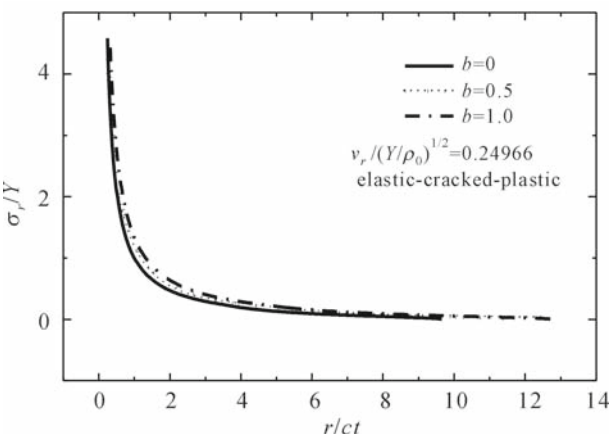

Fig. 12.12. Radial stress versus radius for incompressible material

1.05, where the cracked zone disappears and the response of the material is elastic-plastic.

Figs.12.17 and 12.18 compare the cavity expansion pressures between the elastic-plastic and elastic-crack-plastic responses for compressible materials for $b = 1.0$ (Twin-shear theory), $b = 0.5$ (Median theory) and $b = 0$ (Single-shear theory), respectively.

From Figs.12.17, 12.18, and 12.19, the cavity expansion pressure for elastic-crack-plastic response is lower when the expansion velocity is lower. With the increase of the cavity expansion velocity, the cracked zone disappears and the response of the target becomes elastic-plastic.

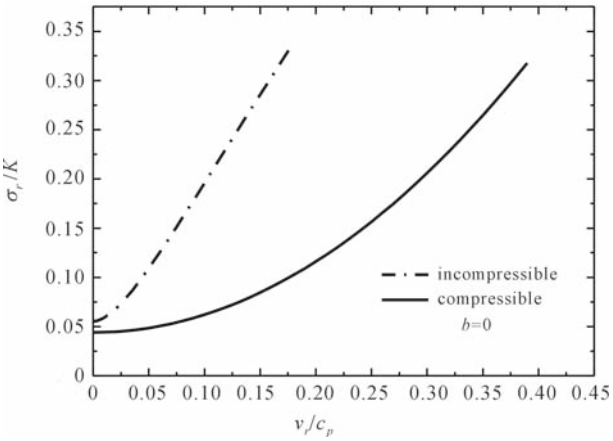

Fig. 12.13. Comparison of radial stress between incompressible and compressible materials ($b = 0$)

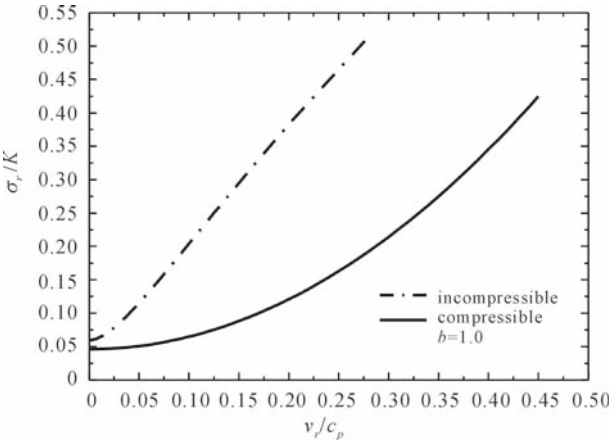

Fig. 12.14. Comparison of radial stress between incompressible and compressible materials ($b = 1.0$)

For compressible materials the curves of the cavity expansion pressure versus cavity expansion velocity can be expressed as a quadric parabola,

$$\sigma_r/K = A_1 + B_1 \left(\frac{v_r}{c_p}\right)^2, \tag{12.97}$$

where v_r is the cavity expansion velocity; A_1 is the quasi-static cavity expansion pressure.

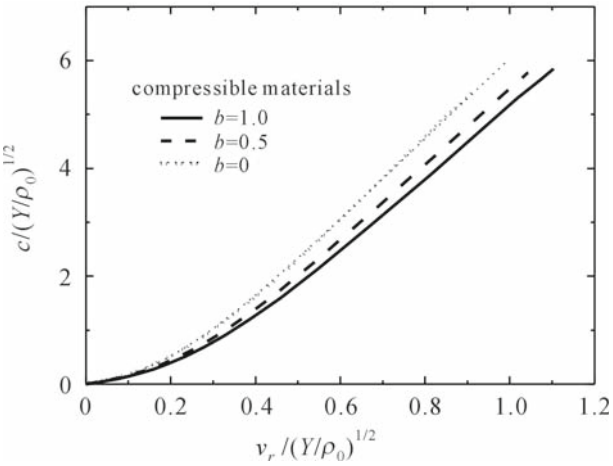

Fig. 12.15. v_r versus c for elastic-crack-plastic response (incompressible materials)

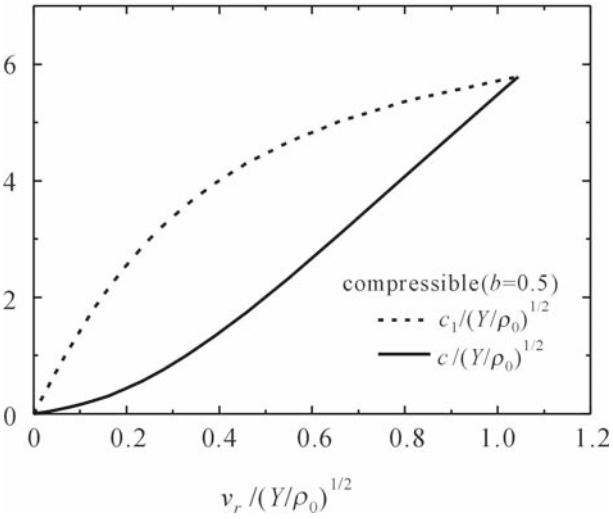

Fig. 12.16. Cavity expansion velocity versus interface velocity (compressible materials, $b = 0.5$)

The coefficients in Eq.(12.97) are listed in Table 12.1 for the elastic-plastic and elastic-crack-plastic responses, respectively, with different unified strength theory parameter b.

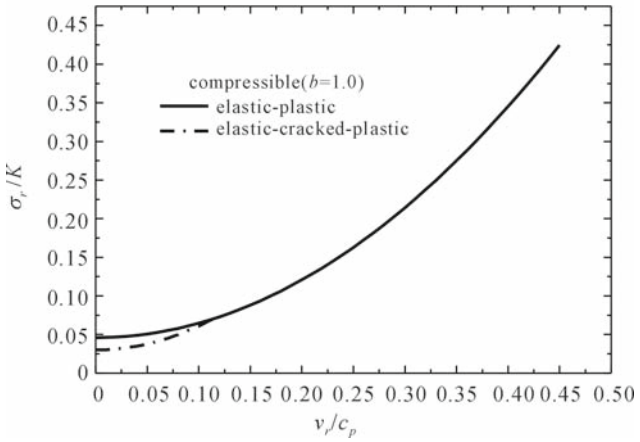

Fig. 12.17. Comparison of cavity expansion velocities between elastic-plastic and elastic-crack-plastic responses (compressible materials, $b = 1.0$)

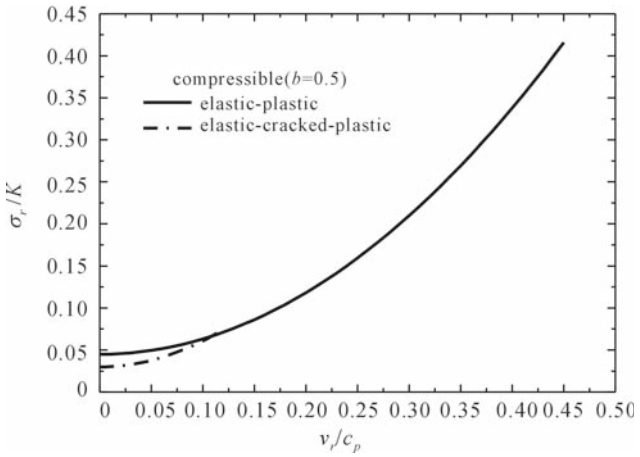

Fig. 12.18. Comparison of cavity expansion velocities between elastic-plastic and elastic-crack-plastic responses (compressible materials, $b = 0.5$)

12.6 Penetration Resistance Analysis

The capabilities of penetration and destruction of a long rod projectile are much higher than those of the old-style armor-piercing projectile since the long rods have a higher length-diameter ratio. The long rod projectiles can be divided into straight-shank type and cone-shank type. According to the shape of warhead the long rod can be categorized into a spherical, ogive, and conical warhead nose, respectively, as shown in Fig.12.20.

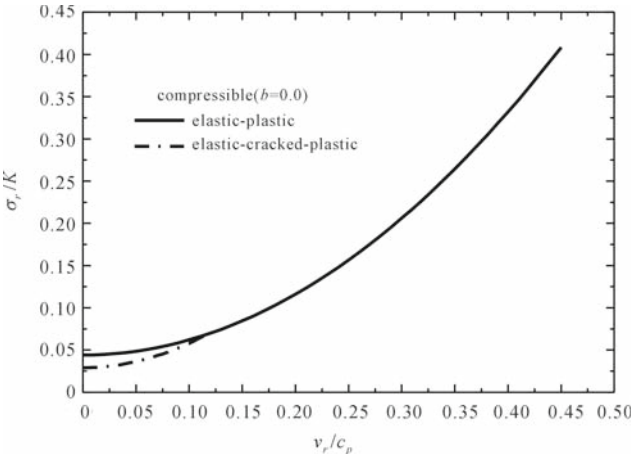

Fig. 12.19. Comparison of cavity expansion velocities between elastic-plastic and elastic-crack-plastic responses (compressible materials, $b = 0$)

Table 12.1. Curve fitting of cavity expansion pressure for compressible materials under elastic-plastic response

Response	Material strength parameter b	A_1	B_1
Elastic-plastic	1.0	0.044	1.80
	0.5	0.045	1.83
	0.0	0.046	1.87
Elastic-crack-plastic	1.0	0.029	2.90
	0.5	0.030	3.02
	0.0	0.031	3.10

Because a long rod impacts and penetrates a target with an impact velocity V_0 and a penetration velocity V_z, the coordination xOz of the target is established as shown in Fig.12.21. The origin is the impacting point of the long rod, the positive z axial is downwards vertically, and the x axial is horizontal. The resistance on the long rod includes the resistance on the warhead and that on the surface of the shank. The resistance on the shank surface is very small and can be omitted because the velocity of the impact and penetration is low (Jones et al., 1993; Bless et al., 1987).

The tractions that resist the penetration are the normal force F_n, and the tangential force F_t. The resistance is analyzed in the following context for

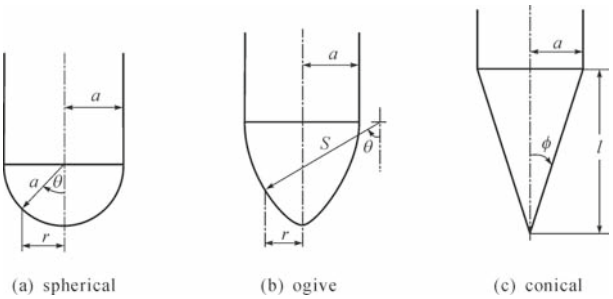

Fig. 12.20. Different head shapes of straight long rods

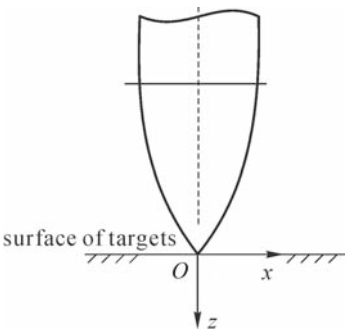

Fig. 12.21. Rod-target system

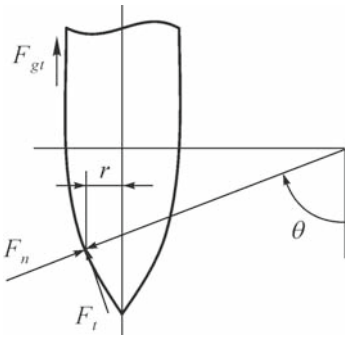

Fig. 12.22. Resistance on the long rod

the ogive-nose projectile. The resistances for other nose shape projectiles can be similarly derived.

For an ogive-nose projectile as shown in Fig.12.20(b) with radius of s, central angle of θ_0,

$$\theta_0 = \sin^{-1}\left(\frac{s-a}{s}\right). \tag{12.98}$$

The normal force on the tiny surface of the warhead is

$$\mathrm{d}F_n = 2\pi s^2 \left[\sin\theta - \left(\frac{s-a}{s}\right)\right] \sigma_r \mathrm{d}\theta. \tag{12.99}$$

The tangential force on the tiny surface of the warhead is

$$\mathrm{d}F_t = 2\pi s^2 \left[\sin\theta - \left(\frac{s-a}{s}\right)\right] \mu\sigma_r \mathrm{d}\theta, \tag{12.100}$$

where σ_r is the principal stress on the warhead, which is also the radial stress on the cavity surface using the cavity expansion theory. μ is the friction coefficient. The value of μ depends on the penetration depth, velocity and the material properties of the rod and the target. Its linear experiential formula is proposed by Bowden and Tabor (1966),

$$\mu = \begin{cases} \mu_d, & V_z \geqslant V_d, \\ \mu_s - \dfrac{\mu_s - \mu_d}{V_d} V_z, & V_z \leqslant V_d, \end{cases} \tag{12.101}$$

where V_d is the critical penetration velocity which can be obtained by trial-and-error; μ_s and μ_d are friction parameters of the targets, which are related to the penetration velocity. For the geomaterials, there are $V_d = 300$ m/s, $\mu_s = 0.5$, $\mu_d = 0.08$ (Bowden and Tabor, 1966).

The radial stress can be written as

$$\sigma_r / K = A_1 + B_1 \left(\frac{\nu_r}{c_p}\right)^2. \tag{12.102}$$

The relation between the cavity expansion velocity and the penetration velocity is

$$V_r = V_z \cos\theta, \tag{12.103}$$

where θ is the angle between the surface normal and the rod axial directions.

Putting Eq.(12.103) into Eq.(12.102),

$$\sigma_r / K = A_1 + B_1 \left(\frac{V_z \cos\theta}{c_p}\right)^2. \tag{12.104}$$

The total resistance on the warhead is

$$F_z = 2\pi s^2 \int_{\theta_0}^{\frac{\pi}{2}} \left[\left(\sin\theta - \frac{s-a}{s}\right)(\cos\theta + \mu\sin\theta)\right] \sigma_r \mathrm{d}\theta. \tag{12.105}$$

Integrating Eq.(12.102) with reference to Eq.(12.105),

$$F_z = \alpha_s + \beta_s V_z^2, \tag{12.106}$$

where

$$\alpha_s = \pi a^2 K A_1 [1 + 4\mu\psi^2(\pi/2 - \theta_0) - \mu(2\psi - 1)(4\psi - 1)^{1/2}], \tag{12.107}$$

$$\begin{aligned}\beta_s = \pi a^2 \rho B_1 \Bigg[& \frac{(8\psi - 1)}{24\psi^2} + \mu\psi^2(\pi/2 - \theta_0) \\ & - \frac{\mu(2\psi - 1)(6\psi^2 + 4\psi - 1)(4\psi - 1)^{1/2}}{24\psi^2} \Bigg].\end{aligned} \tag{12.108}$$

The resistance on rods of other shapes can also be deduced similarly with the replacement of different geometry shape functions based on the shapes of the nose of the rod.

12.7 Analysis and Verification of Penetration Depth

Assuming a long rod is non-deformable during the penetration, with reference to the Newton's second law,

$$m_p \frac{\mathrm{d}V_z}{\mathrm{d}t} = m_p V_z \frac{\mathrm{d}V_z}{\mathrm{d}z} = -F_z = -(\alpha_s + \beta_s V_z^2), \tag{12.109}$$

where α_s and β_s are the shape parameters of the nose; m_p is the mass of the rod.

Integrating Eq.(12.109) with reference to the initial and final conditions, the penetration depth can be deduced,

$$Z_{\max} = \frac{m_p}{2\beta_s} \ln \left[1 + \frac{\beta_s V_0^2}{\alpha_s} \right]. \tag{12.110}$$

The parameters for the target material in Section 12.5 are also applied for the current problem. The parameters used for the long rod are m_p=1.6 kg, s=91.5 mm, a=15.25 mm.

Based on the results of the cavity expansion pressure for compressible materials in Section 12.5, the final penetration depth can be derived for the target material impacted by an ovate straight long rod with a velocity of 300 *sim* 1100 m/s. The analytical results from the current penetration model agree very well with the test data (Forrestal et al., 1996) when the initial velocity is low.

The penetration depths are illustrated schematically in Fig.12.23 for the friction parameters $\mu = 0.1$ and $\mu = 0.2$ respectively. From Fig.12.23 the friction parameter has great influence on the penetration depth. The penetration depth for $\mu = 0.1$ is closer to the test results (Forrestal et al., 1996).

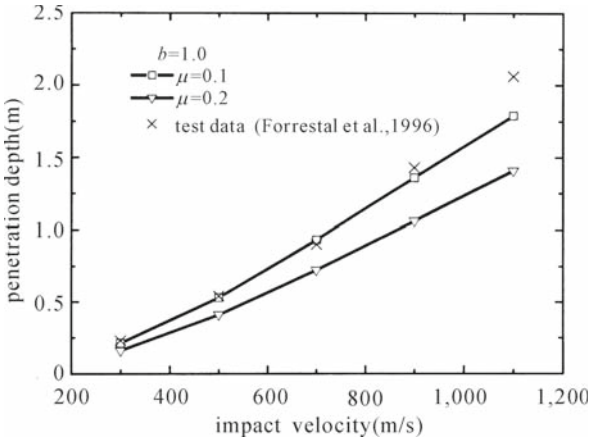

Fig. 12.23. Comparison of penetration depths

Fig.12.24 shows the influence of rod mass on the penetration depth. It is seen that the heavier the rod, the greater the penetration capability.

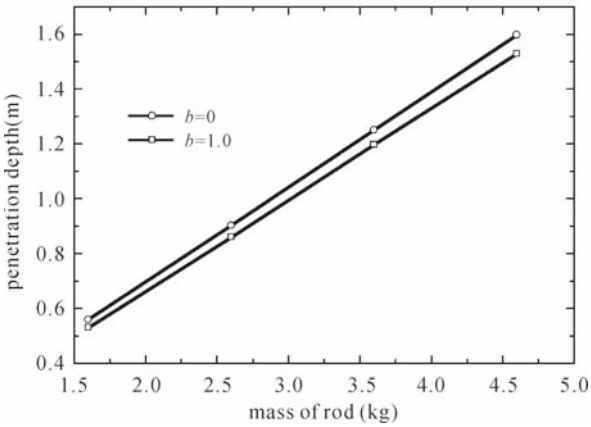

Fig. 12.24. Influence of the rod mass on the penetration depth

The penetration depths are solved for the ovate and spherical warheads with the same shank diameter as that for the ogive-nose projectile as shown

Fig.12.25. It can be seen that the ovate-warhead rod can penetrate deeper than the spherical warhead rod.

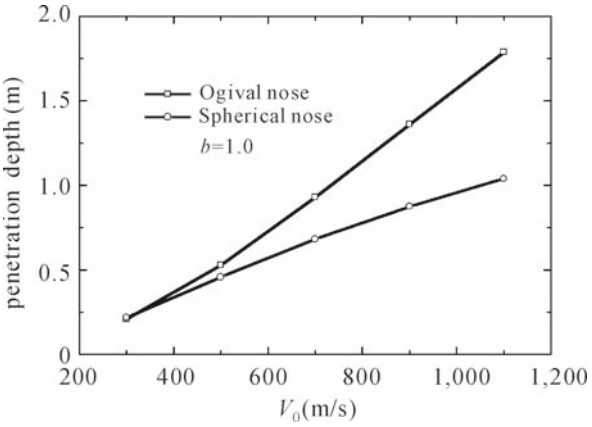

Fig. 12.25. Influence of different shapes of warhead on penetration depth

12.8 Summary

Based on the cylindrical cavity-expansion theory, the unified strength theory is applied as the failure condition for penetration analysis. The cavity expansion pressure is deduced from the elastic-plastic and elastic-crack-plastic responses for incompressible and compressible materials. Assuming the long rods are rigid during the penetration, the penetration depths of rods are obtained and are compared with the test results. The following conclusions are derived:

(1) It is convenient to use the unified strength theory for penetration problems.

(2) When the cavity expansion velocity is low, the target response is elastic-crack-plastic. When the cavity expansion velocity increases to a certain value, the cracked zone disappears and the target responds elastic-plastically. It agrees with the results reported by Forrestal (1997).

(3) The cavity expansion pressure and the penetration depth are different when the different parameter b is used, which represents a different failure criterion. The penetration depth is higher for $b = 0$ than that for $b = 1$. The current solutions agree well with test results in the published literature for low impact velocity cases (Forrestal et al., 1996). However, the predicted penetration depth is smaller than that in the test results when the impact velocity is larger than 1000 m/s.

(4) For a given shape and dimension, the higher the rod mass or the density of the rod material, the deeper the penetration. This may be the underlying reason why those high-density metals are used as warheads for modern weapons.

(5) The shape of a warhead has a significant influence on the penetration depth. When the shank diameter is the same, the ovate-warhead rod can penetrate deeper than the spherical warhead.

References

Bishop RF, Hill R, Mott NF (1945) The theory of identification and hardness tests. The Proc. Phys. Soc. 57(3):147-159

Bless SJ, Rosenberg Z, Yoon B (1987) Hypervelocity penetration of ceramics. Int. J. Impact Eng., 5:165-171

Bowden FP, Tabor D (1966) Friction, lubrication and wear—survey of work during last decade. British Journal of Applied Physics, 17(12):1521-1544

Forrestal MJ, Frew DJ, Hanchak SJ, Brar NS (1996) Penetration of grout and concrete targets with ogive-nose steel projectiles. Int. J. Impact Eng., 18(5):465-476

Forrestal MJ, Tzou DY (1997) Spherical cavity-expansion penetration model for concrete targets. Int. J. Solids Struct., 34(31-32):4127-4146

Forrestal MJ, Zhou DY, Askari E, Longcope DB (1995) Penetration into ductile metal targets with rigid spherical-nose rods. Int. J. Impact. Eng., 16(5/6):699-710

Heuze FE (1990) Overview of projectile penetration into geological materials, with emphasis on rocks. Int. J. Rock Mechanics and Mining Sciences & Geomechanics Abstracts, 27(1):1-14

Hill R (1950) The mathematical theory of plasticity. Clarendon Press, London

Hopkins HG (1960) Dynamic expansion of spherical cavities in metal. In: Sneddon IN, Hill R (eds.) Progress in Solid Mechanics, Vol.1, Chapter III, North-Holland Publ. Co., Amsterdam, New York

Jones SE, Marlow RB, House JW, et al. (1993) A one-dimensional analysis of the penetration of semi-infinite 1100-0 aluminum targets by rods. Int. J. Impact Eng., 14: 407-416

Li JC (2001) Investigation of high velocity long-rod penetration semi-infinite concrete plate. Ph.D. dissertation, Xi'an Jiaotong University (in Chinese, English abstract)

Li JC, Yu MH, et al. (2000) The dynamic investigation of semi-infinite concrete targets penetrated by long rods. Mechanics 2000, Forest Press, Beijing, 519-520.(in Chinese)

Li JC, Yu MH, Gong YN (2000) Dynamic investigation of semi-infinite concrete target penetrated by long rod. In: Proceedings of the 3rd Asian-Pacific Conference. On Aerospace Technology and Science, Beijing University of Aeronautics and Astronautics Press, Beijing, 263-269

Li QM (2005) Penetration of a hard missile. 6th Asia-Pacific Conference on Shock & Impact Loads on Structures, Dec 7-9, 2005, Perth W, Australia, 49-62

Longcope DB, Forrestal MJ (1983) Penetration of targets described by a Mohr-Coulomb failure criterion with a tension cutoff. J. Appl. Mech., 50:327-333

Luk VK, Forrestal MJ (1987) Penetration into semi-infinite reinforced-concrete targets with spherical and ogival noise projectiles. Int. J. Impact Eng., 6(4):291-301

Mastilovic S, Krajcinovic D (1999) Penetration of rigid projectiles through quasi-brittle materials. J. Appl. Mech., 66:585-592

Wang YB (2004) Research in structural impacting problems based on the unified strength theory. Ph.D. dissertation, Xi'an Jiaotong University (in Chinese, English abstract)

Wang YB, Li ZH, Wei XY, Yu MH (2005) Analysis of high-velocity tungsten rod on penetration brittle target. Chinese J. High Pressure Physics, 19(3):257-263 (in Chinese, English abstract)

Wang YB, Zhu YY, Yu MH (2004) Penetration analysis of high-velocity tungsten rod on ceramic targets using unified strength theory. Explosion and Shock Waves, 24(6):534-540 (in Chinese, English abstract)

Wei XY (2002) Investigation of long-rod penetration problems. Ph.D. dissertation, Xi'an Jiaotong University (in Chinese, English abstract)

Wei XY, Yu MH (2002) Analysis of tungsten rod on penetration ceramic targets at high velocity. Acta Armamentarii, 23(2):167-170 (in Chinese, English abstract)

Yu MH (1992) A new system of strength theory. Xi'an Jiaotong University Press, Xi'an, China (In Chinese)

Yu MH (2004) Unified Strength theory and its applications. Springer, Berlin

Yu MH, He LN (1991) A new model and theory on yield and failure of materials under complex stress state. In: Mechanical Behavior of Materials-6, Pergamon Press, Oxford, 3:841-846

Yu MH, He LN, Liu CY (1992) Generalized twin shear stress yield criterion and its generalization. Chinese Science Bulletin, 37(24):2085-2089

Yu MH, Li JC, Zhang YQ (2001) Unified characteristics line theory of spatial axisymmetric plastic problem. Science in China (Series E), English ed., 44(2):207-215; Chinese ed., 44(4):323-331

Yu MH, Ma GW, Qiang HF, et al. (2006) Generalized plasticity. Springer, Berlin

Yu MH, Yang SY, Liu CY, Liu JY (1997) Unified plane-strain slip line theory. China Civil Eng. J. 30(2):14-26 (in Chinese, English abstract)

Zukas JA, Nicholas T, Swift HF, et al. (1982) Impact dynamics. John Wiley & Sons, Inc., New York